Nuclear Engineering and Design 353 (2019) 110274

Contents lists available at ScienceDirect

Nuclear Engineering and Design

journal homepage: www.elsevier.com/locate/nucengdes

Reference numerical database for turbulent flow and heat transfer in liquid metals

A. Shams[a,*], F. Roelofs[a], B. Niceno[b], W. Guo[b], D. Angeli[c], E. Stalio[c], A. Fregni[c], M. Duponcheel[d], Y. Bartosiewicz[d], I. Tiselj[e], J. Oder[e]

[a] Nuclear Research and Consultancy Group (NRG), Petten, The Netherlands
[b] Paul Scherrer Institute (PSI), Villigen, Switzerland
[c] University of Modena and Reggio Emilia (UNIMORE), Modena, Italy
[d] Université catholique de Louvain (UCL), Louvain-la-Neuve, Belgium
[e] Jožef Stefan Institute (JSI), Ljubljana, Slovenia

ARTICLE INFO

Keywords:
Turbulent heat transfer
Liquid metal
Reference database

ABSTRACT

Turbulent heat transfer is a complex phenomenon that has challenged turbulence modellers over various decades. In this regard, in the recent past, several attempts have been made for the assessment and further development/calibration of the available turbulent heat flux modelling approaches. One of the main hampering factors with respect to the further assessment of these modelling approaches is the lack of reference data. In the framework of the EU SESAME and MYRTE projects, an extensive effort has been put forward to generate a wide range of reference data, both experimental and numerical, to fill this gap. In that context, this article reports the numerical database that has been generated within these projects for various liquid metal flow configurations in different flow regimes. These high fidelity numerical data include seven different flow configurations: a wall-bounded mixed convection flow at low Prandtl number with varying Richardson number (R_i) values; a wall-bounded mixed and forced convection flow in a bare rod bundle configuration; a forced convection confined backward facing step (BFS) with conjugate heat transfer; a forced convection impinging jet for three different Prandtl fluids corresponding to two different Reynolds numbers of the fully developed planar turbulent jets; a mixed-convection cold-hot-cold triple jet configuration corresponding to $R_i = 0.25$; an unconfined free shear layer for three different Prandtl fluids; and a forced convection infinite wire-wrapped fuel assembly. These high-fidelity numerical databases will serve the further development of turbulent heat transfer models by providing unique, new and detailed data for the thermal-hydraulic behaviour of liquid metals in various flow configurations.

1. Introduction

Turbulent heat transfer is a complex phenomenon and has challenged turbulence modellers for various decades. On top of that, for the application to liquid metal cooled nuclear reactors it even becomes more complicated. This has already been discussed several times in literature, e.g. by Grotzbach et al. (2013), Shams et al. (2019), Roelofs et al. (2015) and Shams (2017, 2018, 2019). In short summary, one can say that the most often applied Reynolds analogy between momentum and heat transfer is not valid for application to liquid metals due to the fact that the thermal conductivity of liquid metals is relatively high and the Prandtl number is relatively low. It has been shown that due to this variation in the properties of the fluid, application of the Reynolds analogy will lead to inaccurate results. The challenge is to find a robust model which can be used in engineering simulations. Since application to liquid metal cooled reactors requires to deal with the complex flow and heat transport in a large liquid metal pool, the model should be able to deal preferably with different flow regimes simultaneously.

In June 2013, European liquid metal modelling experts gathered in Amsterdam to discuss the current status and the future outlook. At that time, the available models and reference data were limited to forced convection liquid metal flows in geometrically relatively simple cases like channel flows and the flow over a channel with one wavy wall (Roelofs et al., 2014). It was concluded that most turbulence models give sufficiently good results for forced convection in the geometrically simple test cases assessed thus far. Therefore, further work should focus on mixed and natural convection and for geometrically complex cases. However, for such cases, new reference data is required to extend the

---

* Corresponding author.
E-mail address: shams@nrg.eu (A. Shams).

https://doi.org/10.1016/j.nucengdes.2019.110274
Received 29 April 2019; Received in revised form 8 August 2019; Accepted 9 August 2019

validation base. To this purpose, the following suggestions were identified for extension of the validation base: mixing jets, flow separation, mixed convection around single pin, and rod bundle cases. This has led to the establishment of a common and complementary data production program in two new European collaborative projects, the Horizon 2020 MYRTE and the SESAME project. The data production is a combination of an experimental and a numerical data production program. Obviously, the experimental data production program is targeted. However, due to difficulties in such a program related to measurement limitations and costs, also an extensive numerical data production program was initiated. It should be noted, that in such a numerical data production program, numerical techniques are being used which do not employ models to capture the turbulent behaviour of a fluid. Apart from that, such numerical reference data is extremely valuable for model development and validation as the conditions are well controlled and apart from hardware limitations, in principle, all locations are accessible at all times of simulation.

This paper presents the collaborative European effort to set up a numerical data production program as mentioned before resulting in a completely new numerical reference database. The cases dealing with various flow regimes, various geometrical complexities and various liquid metals will be introduced on a case to case basis. The following seven cases are discussed:

1. a wall-bounded mixed convection flow at low Prandtl number with varying Richardson number values
2. a forced convection confined backward facing step for three different Prandtl fluids
3. a forced convection impinging jet for three different Prandtl fluids corresponding to two different Reynolds numbers of the fully developed planar turbulent jets
4. a mixed-convection cold-hot-cold triple jet configuration corresponding to a Richardson number of 0.25
5. an unconfined free shear layer with three different Prandtl fluids
6. a wall-bounded forced and mixed convection flow in a bare rod bundle configuration
7. a forced convection flow in an infinite wire-wrapped fuel assembly

The resulting numerical reference database aims at serving the further development and validation of turbulent heat transfer models by providing unique, new and detailed data for the thermal-hydraulic behaviour of liquid metals in various flow configurations.

2. Mixed convection channel flow

2.1. Flow configuration

A sketch of the flow configuration selected to study the mixed convection is depicted in Fig. 1, which is horizontal channel flow. The Prandtl number of considered working fluid, which is a liquid metal, is 0.025. The top and the bottom walls are heated uniformly at a certain temperature. The temperature of the cold wall, at the top, is fixed at T_c and the hot wall, at the bottom, has a relatively higher temperature T_h.

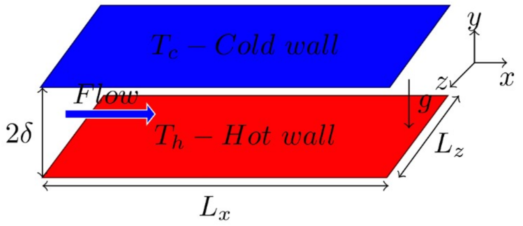

Fig. 1. Sketch of the mixed convection channel flow.

Table 1
Simulation parameters of the mixed convection case.

Boundary conditions	Periodic (x, z directions), no-slip (y-direction)
Mesh Size	$512 \times 257 \times 512$
Computational domain	$10\pi\delta \times 2\delta \times 4\pi\delta$ ($\delta = 1$)
Richardson number	0, 0.25, 0.5 & 1
Reynolds number	4667
Prandtl number	0.025
Grashof number	o, 5.1×10^6, 1×10^7, 2.13×10^7
Friction Reynolds number	151, 171, 183, 196
Δx^+, Δy^+, Δz^+	$R_i = 0$: 9.3, 1.2, 3.7 $R_i = 0.25$: 10.5, 1.3, 4.2 $R_i = 0.5$: 11.2, 1.4, 4.5 $R_i = 1$: 12, 1.5, 4.8

The difference of the temperature $\Delta T_{hc} = (T_h - T_c)$ between the two walls induces buoyancy force throughout the flow field. The acceleration acts downward along the y-direction because of gravity. The streamwise, wall-normal and spanwise coordinates are presented by x, y, z, respectively. In total, four different Richardson numbers ($R_i = 0$, 0.25, 0.5, 1.0) are simulated. The simulation parameters of this mixed convection study are shown in Table 1. Following the work of Tiselj (2014), the selected computational domain is kept relatively large, compared to a typical turbulent channel flow case with unity Pr fluid, in order to capture the large scale structures in the temperature field. Accordingly, a relatively large computational resource is consumed to perform the simulation. As a result, 2048 cores from Cray XC40 are used for parallel computing and 0.75 million core hours are consumed.

2.2. Numerical methodology

The simulation tool used in this study is an open source Computational Fluid Dynamics (CFD) solver named Incompact3d (https://www.incompact3d.com/). It is developed at Imperial College London and the University of Poitiers by Laizet and Lamballais (2009) and Laizet and Li (2011). It uses six-order-accurate finite difference compact scheme for spatial discretization and a hybrid second order Crank-Nicolson as well as Adam-Bashforth as the temporal scheme (Dairay et al., 2014; Flageul et al., 2017). Because the temperature difference between the two walls is small, the thermo-physical properties of the fluid are uniform and the common Oberbeck-Boussinesq (OB) approximation is used.

2.3. Selected results

Fig. 2 shows the statistics of mean and the RMS of three velocity components. It indicates that turbulence is strongly enhanced by buoyancy, i.e. with the increasing R_i number. The skin friction is also increased with the increase of R_i number and it causes the velocity boundary layer much thinner.

Fig. 3 shows the profiles of mean temperature and its RMS along with the turbulent heat fluxes. It shows that temperature fluctuations are distributed more homogeneously and mixing is more effective in the bulk region of the channel. The energy transport in streamwise is enhanced by small buoyancy force. When the buoyancy becomes stronger, better mixing happens, which consequently decreases the streamwise turbulent heat flux.

In Fig. 4, the profiles of the turbulent Prandtl number Pr_t are given. It can be seen that for the forced convection ($R_i = 0$) case, the value of the Pr_t is much larger. Whereas for mixed convection regime, the values are globally decreased and the maximum value is close to 1 which appears in the viscous sublayer. In the center of the channel, Pr_t decreases towards zero. This proves that the momentum eddy diffusivity is relatively stronger in the region close to the wall and heat transfer eddy diffusivity is dominant in the center of the channel because of

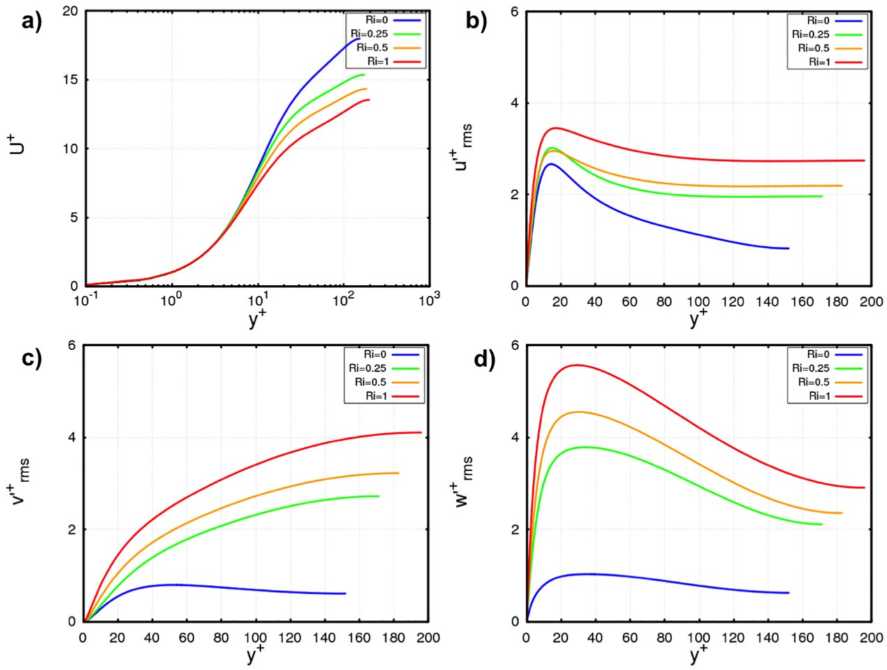

Fig. 2. (a) Mean velocity profiles (b) The RMS of u-velocity component (c) The RMS of v-velocity component (d) The RMS of w-velocity component.

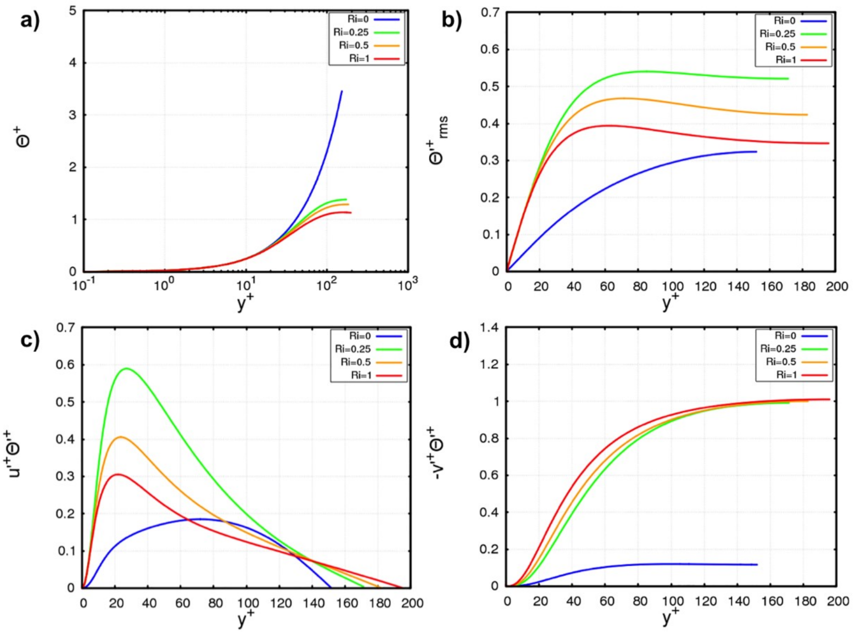

Fig. 3. (a) Mean temperature profiles (b) The RMS of temperature fluctuations (c) Streamwise turbulent heat fluxes (d) Wall normal turbulent heat fluxes.

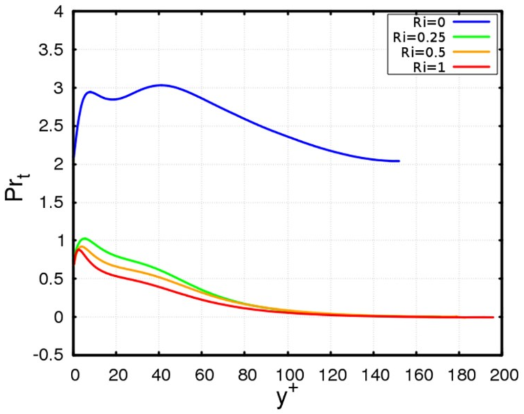

Fig. 4. Evolution of Turbulent Prandtl number.

enhanced mixing by buoyancy. This is an important finding and highlights the limitations of Reynolds analogy, which is based on a constant Pr_t and has been adopted by many RANS based CFD codes to simulate the heat transfer phenomenon in low Prandtl fluid (Kasagi and Ohtsubo, 1993; Kays, 1994 Shams et al., 2014).

3. Backward Facing Step (BFS)

3.1. Flow configuration

A sketch of the selected BFS configuration is given in Fig. 5. The simulated domain is 3D and is limited by walls in both spatial directions perpendicular to the general direction of the flow. The expansion ratio, which is the ratio between the surface of the outflow and surface of the inflow of the step, is equal to 2.25. The step and the lower walls are 0.25 dimensionless units thick and are thermally connected to the fluid domain. The lower step wall is internally heated. Buoyancy effects are not considered in the present simulation. Buoyancy would add considerable computational effort to the simulation and its inclusion is planed after the execution of the liquid metal experiments at KIT.

The Reynolds number, based on mass flow rate $\dot{m}$ and hydraulic diameter of the inflow is equal to 7089. It is calculated with the formula:

$$Re = \frac{2\dot{m}}{(L_y + L_z)\mu} \tag{1}$$

where L_z and L_y are dimensional width and height of the inflow, respectively and μ is the dynamic viscosity of sodium. The Prandtl number for the present case is set to $Pr = 0.005$, which is roughly the Pr number of liquid sodium at around 550 K. The ratio of thermal diffusivities between the fluid and the wall has been set to 10, which roughly corresponds to the ratio of thermal diffusivities between liquid sodium and steel. Similarly, the ratio of thermal conductivities of the fluid and the solid material are set to 3.

3.2. Numerical methodology

The Navier-Stokes system of equations is solved for the fluid domain. Additionally, an internal energy equation is solved in both fluid and solid domain. The temperature does not appear in the momentum equation and thus is considered as a passive scalar. The fluid and solid domains are coupled with the conjugate heat transfer model. In the lower wall in (as shown in Fig. 5) a heat source term is present in the internal energy equation. The boundary condition at the solid edges of the fluid domain is a no-slip boundary condition. At the outflow, a constant pressure boundary condition was applied. To produce a fully turbulent inflow boundary condition, the velocity field is taken from a plane parallel to the inflow plane 6 dimensionless units downstream. The streamwise velocity component is renormalized so that the average stream velocity is equal to 1. The resulting velocity field is then imposed as the inflow boundary condition, following the concept of recycling boundary conditions. The temperature at the inlet is set to zero. The outer walls are thermally adiabatic, including the outflow.

The DNS is performed using the code Nek5000 (Fischer et al., 2010). This is an open source code developed by Argonne National Laboratory. Nek5000 is an implementation of the spectral element method; a high-order finite element method for solving partial differential equations. Similar to the procedure with finite element techniques, the computational domain is divided into elements. However, within each element, a solution is sought at points that are distributed through the element. These points are not distributed uniformly but are clustered at the edges of the element. This approach retains the high-order (spectral) accuracy of spectral methods and maintains the geometric flexibility of finite-element techniques.

The computational domain is divided into approximately 153 000 elements from which approximately 143 000 are in the fluid domain. The size of the elements varies in the wall normal directions, but remains constant in the streamwise direction. The 7th degree collocation points in each direction within each element has been used to perform this simulation. This results in approximately 31 million unique points in the domain.

3.3. Selected results

The simulation is performed on 256 CPUs for more than half a year. The part of simulation where averaging was performed took approximately 1 million CPU-hours. Approximately, 8.5 million time steps are used to produce the average profiles.

Fig. 6 shows the iso-contours of streamwise average velocity through the middle of the domain (plane z = 1.8). Upstream of the step, the maximum value of velocity is achieved in the middle of the domain

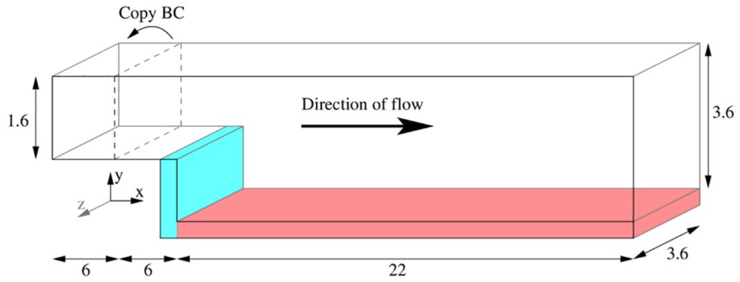

Fig. 5. Sketch of the BFS domain with solid walls. The walls are 0.25 units thick. The blue part of the wall is not heated while the red part has an internal heating.

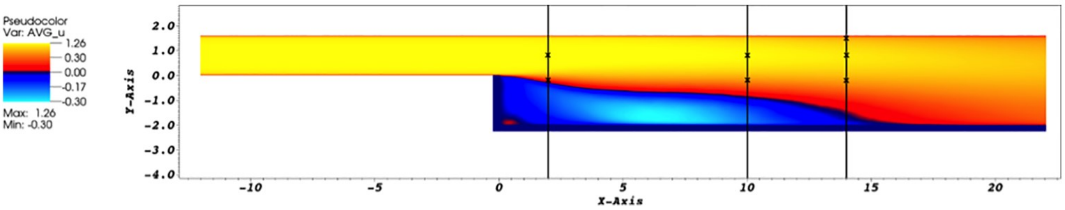

Fig. 6. Time averaged iso-contours of x-component of velocity through the middle of the domain (plane z = 1.8).

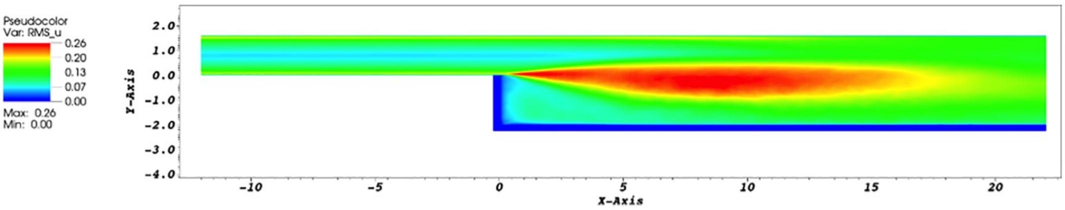

Fig. 7. Iso-contours of RMS of stream-wise velocity component through the middle of domain (plane z = 1.8).

and is equal to 1.26 dimensionless velocity units. Whereas, downstream of the step, the maximum value of the stream-wise velocity component drops. Moreover, the velocity component has a different sign after the step and flows in the opposite direction of the general flow, i.e. recirculation zone. At around x = 15, the velocity changes the direction in the direction.

Fig. 7 presents the fluctuations of stream-wise velocity component through the middle of the domain (plane z = 1.8). Upstream of the step, the velocity fluctuations have a shape that is typical for the turbulent channel flows. Downstream of the step, the velocity fluctuations start rising and reach the maximum of 0.26 approximately 8.5 dimensionless units downstream of the step, and approximately 1.62 above the lower wall. In this figure, the solid walls are clearly visible, as the velocity fluctuations are 0.

Fig. 8 shows the time average temperature field. The highest temperature is reached at the bottom wall, approximately 2.25 dimensionless units downstream of the step.

Fig. 9 displays the temperature fluctuations in the middle of the domain. The penetration of the fluctuations into the solid walls is clearly visible. The thermal fluctuations are lowest at the position where the temperature is highest (as shown in Fig. 8). The thermal fluctuations have a local maximum immediately downstream of the step. It must be noted that the thermal fluctuations do not coincide with the fluctuations of velocity.

Fig. 10 shows the average temperature distribution at the lower wall. The solid magenta line shows the region where the average streamwise velocity changes its sign. From the step wall towards the outflow, the average streamwise velocity changes the sign three times. At the outflow, it is directed towards the outflow. The minimum temperature is reached at the side walls (upper and lower side in 10). From this figure, the shape of the recirculation zone can also be observed. The flow reattaches at around 15.8 dimensionless units downstream of the step.

Fig. 11 shows the evolution of mean velocity and temperature and their respective RMS's along the selected profile lines from the domain. The lines and dots marked in Fig. 6 show position, where the data is obtained. The seven points marked with SU are obtained by averaging the data from monitor points, while the three lines are obtained by producing average fields. The sampling error of two standard deviations (2σ) is shown for each point. The probability that the real average and its estimation differ for less than 2 standard deviations is 95%. As this method can be applied for any statistical quantity, accordingly this simulation is able to estimate the sampling error for the mean quantities, the fluctuations of these quantities and for the cross products of these fluctuations (Reynolds stresses and turbulent heat fluxes). The sampling error was estimated with the open-source library, (see Oliver et al., 2014).

4. Impinging jet

4.1. Flow configuration

The setup of the plane impinging jet consists of two infinite parallel flat plates where the top plate is split by a slit through which fluid is injected to form the jet, which impinges on the bottom plate. The problem is simulated in a rectangular box where the top ($y = H$) and bottom ($y = 0$) surfaces coincide with the walls and the top surface also contains the slit ($y = H$ and $-B/2 < x < B/2$). In the mean flow direction, far away from the jet, at $x = -L/2$ and $L/2$, convective outflow boundary conditions are used, whereas the flow is considered periodic

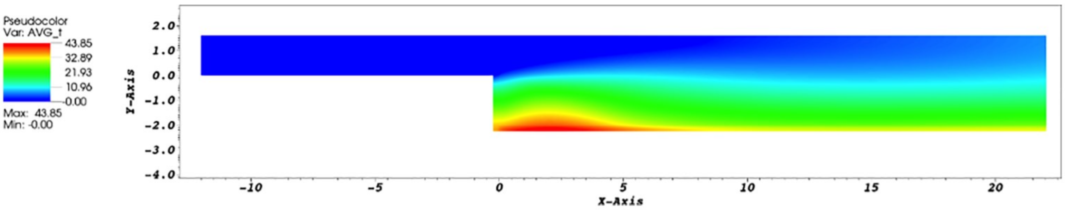

Fig. 8. Time averaged iso-contours of temperature through the middle of the domain (plane z = 1.8).

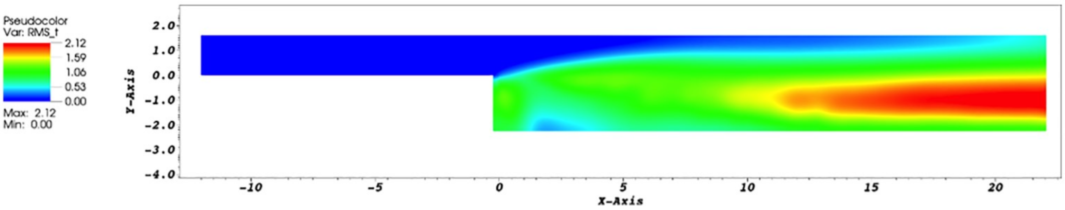

Fig. 9. Iso-contours of RMS of temperature through the middle of domain (plane z = 1.8).

in the spanwise direction (z), in which the domain length is W. This configuration is sketched in Fig. 12.

The top and bottom walls are isothermal, so that $u_i = 0$ and $T = T_w$ when $y = 0$ and when $y = H$ and $|x| \geqslant B/2$. In the slit ($y = H$ and $|x| < B/2$), the inlet jet profile is imposed. In terms of different inflow boundary conditions, two cases are considered:

–flat laminar profile: $(u, v, w) = (0, -U, 0)$,
–fully developed turbulent profile: $u_i(x, H, z) = u_{i,channel}(x, y_0, z)$,

However in both cases, the jet is isothermal $T = T_j$. In the turbulent case, this indeed corresponds to the asymptotic solution of the case with isothermal walls at T_j. The temperature difference between the jet and the walls is $\Delta T = T_j - T_w$. The channel flow solution $u_{i,channel}$ is extracted from an arbitrary plane $y = y_0$ of an auxiliary channel flow simulation running simultaneously with the main jet simulation. The flow can be characterized by the Reynolds number based on the jet mean velocity U and the jet width B: $Re = \frac{UB}{\nu}$, with ν, the kinematic viscosity. This Re is also the bulk Reynolds number of the auxiliary channel, which can also be characterized by the friction Reynolds number $Re_\tau = \frac{\bar{u}_\tau (B/2)}{\nu}$, where $\bar{u}_\tau = \sqrt{\bar{\tau}_w/\rho}$ is the friction velocity, with $\bar{\tau}_w$ the mean wall shear stress. In total, three cases are simulated: the laminar inlet at $Re = 4000$ (L4000), the turbulent inlet at $Re = 4000$ (T4000) and the turbulent inlet at $Re = 5700$ (T5700). For the inlet channel, the $Re = 4000$ and 5700 cases correspond to $Re_\tau = 133$ and 181 respectively. The temperature field, characterized by the Prandtl number $Pr = \nu/\alpha$, was simulated for $Pr = 1 - 0.1 - 0.01$ in all cases.

The impinging jet is also characterized by the dimensionless jet-to-surface spacing, also called Aspect Ratio $AR = H/B$. In the previous DNS, Hattori and Nagano (2004) considered the case $AR = 2$ (and $Re = 4560$) whereas Jaramillo et al. (2012) used $AR = 4$ (and $Re = 20000$). A higher aspect ratio may be desirable in order to be closer to a free impinging jet, while low AR cases are more confined. However, high AR cases are very expensive because they also required longer domains: Jaramillo et al. (2012) showed that, for $AR = 4$, the domain must be at least $40B$-long on each side of the jet so that the outflow boundaries have a negligible effect on the recirculation region. Furthermore, increasing AR also increases the physical time required for a perturbation to leave the domain since the mean velocity between the plates, towards the outflow boundaries, is $U/(2AR)$. Therefore, a small aspect ratio case is considered here: $AR = 2$, similarly to Hattori and Nagano (2004), but with a much longer domain so that the outflow has negligible influence on the jet region: $L/B = 80$, as proposed by Jaramillo et al. (2012) for the $AR = 4$ case, which is thus conservative in the present case.

4.2. Numerical methodology

The Navier-Stokes equations for incompressible flows and the energy equation, both with constant coefficients, are solved using an in-house 4th order finite difference solver which uses a fractional-step method. The equations are discretized in space using the fourth order finite difference scheme of Vasilyev (2000), which is such that the discretized convective term conserves the discrete energy on Cartesian stretched meshes. The Poisson equation for the pressure is solved using a conjugate gradient solver with an efficient parallel multigrid preconditioner. The equations are integrated in time using a second order Adams-Bashforth time-stepping. At low Prandtl number, subtime-stepping is used for the temperature equation because of the very small heat conduction time-scale which is more stringent than the convective time-scale, i.e. the CFL condition.

The main parameters of the simulations are given in Table 2. The final meshes were obtained after several preliminary simulations to adjust and optimize the local grid sizes. The smallest Δx cells are located in the shear-layer region of the jet. The minimum size was determined from the near-wall resolution of the auxiliary channel flow. The axial mesh size increases very slowly in the region $1 < x < 10$, where most of the jet-wall interaction occurs. Then, the mesh size increases significantly up to the outflow. In the wall-normal direction, the mesh is refined close to both walls but preferentially towards the lower wall where the largest wall-fluxes are expected. For the auxiliary channel flow simulation used to generate the inflow data, the domain size is the same as that used by Kim et al. (1987) at $Re_\tau = 180$ (i.e. $L_x/\ B\times\ L_y/\ B\times\ L_z/B = 2\pi \times 1 \times \pi$) and the resolutions are typical of channel flow DNS simulations (Kim et al., 1987; Moser et al., 1999): $\Delta x^+_{max} < 13.0$, $\Delta y^+_{min} < 0.7$ and $\Delta z^+_{max} < 9.0$, in conventional channel flow axis.

The time-step of the simulations are such that $CFL_{max} < 0.15$ in all directions. The time-steps Δt U/B $= 7.5\times 10^{-4}$ and 5.0×10^{-4} for the Re $= 4000$ and 5700 cases, respectively.

The characteristic time of the jet is B/U while the dimensionless time required for a perturbation to travel from the jet to one outflow is of the order of $\frac{t_L U}{B} = \frac{2AR\,L}{U}\frac{U}{B} = 160$. The simulations were always started from the results of another preliminary or production simulation. The

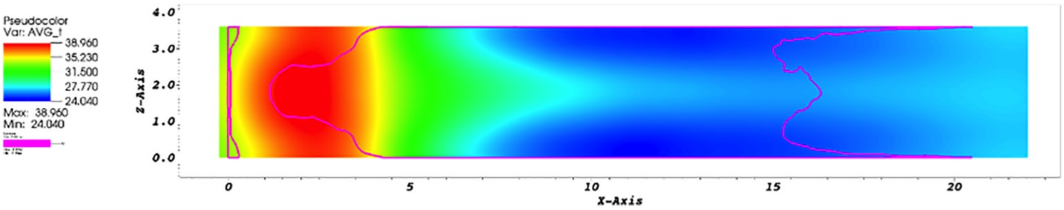

Fig. 10. Time averaged temperature at the lower wall (plane z=-2).

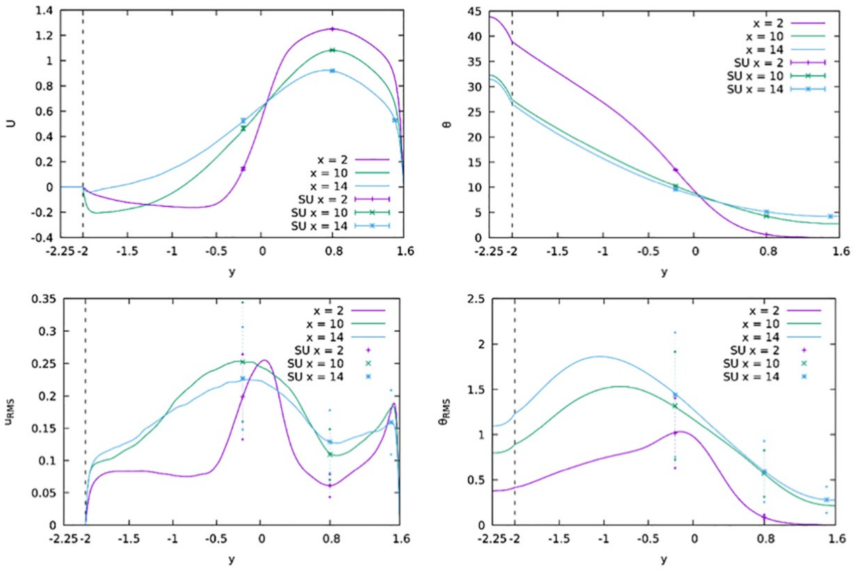

Fig. 11. Selected profiles through the middle of the domain (z = 1.8) of time averaged (top-left) streamwise velocity, (top-right) temperature, (bottom-left) RMS of streamwise velocity, and (bottom-right) temperature fluctuations.

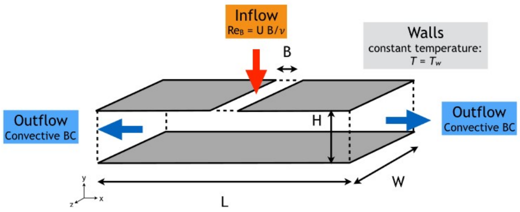

Fig. 12. Sketch of the computational setup.

simulations were then run for at least $\frac{t_L U}{2B}$ before statistics were gathered so that the region of interest near the jet has reached a statistically steady state. The averaging times were $t_{avg} U/B = 99$, 521 and 163 for the L4000, T4000 and T5700, respectively.

4.3. Selected results

Instantaneous visualizations of the flow in a vertical (x-y) plane through the domain are presented in Figs. 13 for the L4000 and T5700 cases. The spanwise vorticity ω_z and the temperature fields at $Pr = 1$ and 0.01 are displayed. In the L4000 case, the uniform inlet profile of the jet can be observed which results in a large potential core. The shear layers at the boundary of the jet only become unstable after the jet is deflected by the presence of the lower wall. Thin boundary layers develop on the lower wall, starting from the stagnation point in the center of the jet. They become turbulent around $x/B = 4$, where the whole deflected jets also transition to turbulence. The effect of the Prandtl number on the different temperature fields is also significant as the gradients are smoothed as the Prandtl decreases. At $Pr = 1$, the core jet at T_j is well visible and only starts to diffuse around $x/B = 4$ when the flow becomes turbulent. At $Pr = 0.01$, the temperature already diffuses in the vertical jet so that no clear region of T_j is visible. Only very weak turbulent fluctuations can be observed. The thermal boundary layers on the bottom wall, being at T_w, are also much thicker at the lowest Pr, even at the stagnation point. The $Pr = 0.1$ case (not shown) is the intermediate between the two other cases: a core at the jet temperature can be observed even after the impingement and turbulent structures are well visible, yet all the gradients are much smoother compared to the $Pr = 1$ case.

In the T5700 case (Fig. 13), the turbulent fluctuations in the jet are well visible at the inlet in the vorticity field. This results in an enhanced mixing of the jet which is already well-mixed after the impingement, at around $x/B = 3$. Consequently, for the temperature at $Pr = 1$, the isothermal core at T_j does not penetrate as far as in the L4000 case, as it mixes faster. At lower Pr, the differences are less pronounced because of the smoothing effect by the higher molecular diffusivity. Some Kelvin-Helmholtz-like roll-ups are visible in the high shear regions of the vertical jet.

The averaged friction coefficient C_f on the bottom wall is shown in Fig. 14. The C_f curves start at zero at the stagnation point, reach a maximum close to $x/B = 1$ and then decrease to reach a plateau corresponding to the fully developed flow between the two walls. Yet, between $x/B = 4$ and 5 depending on the case, the curves exhibit a plateau, or at least a flatter region, before decreasing faster again. In the

Table 2
Simulation parameters.

	Re_B	Pr	$L/B \times H/B \times W/B$	$N_x \times N_y \times N_z$	Inlet
L4000	4000	1.0–0.1–0.01	$80 \times 2 \times \pi$	$2048 \times 144 \times 128$	flat laminar
T4000	4000	1.0–0.1–0.01	$80 \times 2 \times \pi$	$2048 \times 144 \times 128$	fully turbulent
T5700	5700	1.0–0.1–0.01	$80 \times 2 \times \pi$	$2560 \times 192 \times 128$	fully turbulent

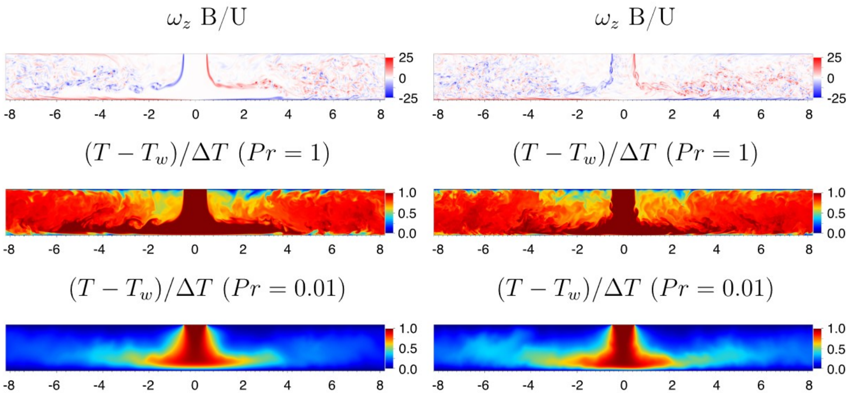

Fig. 13. Visualizations of the instantaneous flow field in an arbitrary $x-y$ plane: L4000 Case (left) and T5700 case (right). Only the region $|x|/B < 8$ is shown.

L4000 case, the end of the plateau is located at $x/B = 6$, which corresponds to the deceleration of the jet and the transition to turbulence of the thin boundary layers developing on the plate. For the turbulent inlet at the same Reynolds number (T4000), the friction coefficient is much larger in the whole region before $x/B = 6$, where the curves come closer to each other. The curves almost collapse when the boundary layers transition and the friction then does not depend on the initial state of the jet. When the *Re* number is increased (T5700), the *Cf* decreases, as expected in boundary layers, but the shape of the curve is globally similar to the $T4000$ case, even though the bump is located slightly further, around $x/B = 5$, compared to 4 in the T4000 case.

The heat flux at the lower wall is presented in the form of the mean Nusselt number *Nu* in Fig. 14. For the Nusselt number at $Pr = 1$ in the L4000 case, the laminar-turbulent transition leads to a secondary peak whose maximum is located at $x/B = 6$. However, in the T4000 case, the secondary maximum is not present because the *Nu* values before $x/B = 6$ are significantly increased with a small plateau around $x/B = 4$. Yet, the L4000 and T4000 curves collapse almost exactly for $x/B > 6$. Again, this increase is due to the enhanced mixing by the vortical structures present near the bottom wall. The plateau is located where these structures start to breakdown. Then, when the boundary layers have transitioned, the heat flux is identical in both laminar and turbulent cases. The T5700 yield higher *Nu* values but with a very similar shape as the T4000 case, even though the plateau then ends around $x/B = 4.5$. It can be observed in Fig. 14 that the secondary peak is not present in the *Nu* profiles at a lower *Pr*, in all three cases. However, an increase of *Nu* close to the stagnation region can be seen between the L4000 and the T4000 at $Pr = 0.1$ and also at $Pr = 0.01$. When *Re* is increased, as in the T5700 case, the shape of the curve is not modified but the *Nu* values increase, as expected in forced convection problems.

The mean velocity profiles at various stations are plotted in Fig. 15. The mean velocity profiles of the L4000 simulation show the potential core at $x/B = 1$ and 2 which is completely diffused at $x/B = 4$. The recirculating region is well visible with the reattachment taking place around $x/B = 9$, and a little further in the T5700 case. The mean profiles of the T4000 and T5700 are very close to each other. At $x/B = 1$, they do not exhibit a maximum in the shear layer and the shear layer is wider than in the L4000 case. Yet, the maximum velocity in the wall jet is larger in the turbulent cases and very close to *U*. At around $x/B = 4$, the mean profiles of the L4000 and T4000 cases almost collapse except very close to the lower wall, since the wall shear stress is still different. At the last stations, $x/B =$ 6–9, the maximum velocity of the T5700 case becomes larger than that of the $Re = 4000$ cases, as the wall jet diffuses more slowly.

The mean temperature profiles are shown in Fig. 16. As already observed in Fig. 13, the low Prandtl case ($Pr = 0.01$) does not exhibit a core region at the jet temperature T_j, as the vertical jet is already much diffused. The $Pr = 1$ profiles, especially for L4000, exhibit an isothermal core at T_j. The temperature gradients at $Pr = 0.01$ are obviously much weaker than at higher *Pr*. At $x/B = 1$ the mixing region is well visible at $Pr = 1$ whereas, at $Pr = 0.01$, the temperature decreases more gradually between the maximum in the jet towards the upper wall temperature. The temperature profiles in the three cases (L4000, T4000 and T5700) are all very similar, except at the first stations where the mixing layer is thinner in the L4000 case. The temperature profiles reach a developed shape much faster than the velocity, as the temperature profiles at $x/B = 7 - 8 - 9$ are very similar even though the

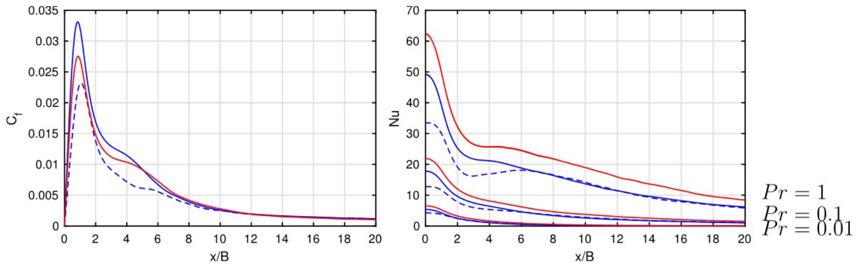

Fig. 14. Mean friction coefficient $C_{f,x} = \frac{\tau_{w,x}}{\frac{1}{2}\rho U^2}$ (left) and mean Nusselt number $Nu = \frac{q_w}{\frac{k}{B}\Delta T}$ (right) on the bottom wall: L4000 (blue dash), T4000 (blue solid) and T5700 (red). (For interpretation of the references to colour in this figure legend, the reader is referred to the web version of this article.)

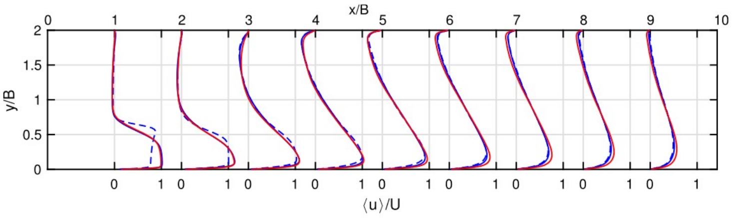

Fig. 15. Mean axial velocity u/U : L4000 (blue dash), $T4000$ (blue solid) and $T5700$ (red). (For interpretation of the references to colour in this figure legend, the reader is referred to the web version of this article.)

flow is not reattached yet and thus clearly not fully developed. The temperature in the T5700 case is then slightly higher than in the other cases.

5. Triple jet

5.1. Flow configuration

A sketch of the triple jet configuration is provided in Fig. 17. The jets have equal mean velocities $U_h = U_c$ but the temperature of the central stream T_h is higher than that of the lateral jets T_c. The jet exits are spaced by 2.5 times their width d. Liquid Lead-Bismuth Eutectic alloy (LBE) is the working fluid. A typical working temperature for LBE in nuclear reactor applications is $T_{\text{ref}} = 220°C$ for which the Prandtl number is $\Pr = 0.031$. Values of the Reynolds and the Grashof numbers are set to $\text{Re} = 5000$ and $\text{Gr} = 6.25 \times 10^6$, respectively. Note that Re is five times lower than in the PLAJEST experiment by Kimura et al. (2007) and other previous numerical studies, (see for example Jung and Yoo, 2004; Yu et al., 2017). The lower Reynolds number selected for the present study allows for a detailed DNS investigation of the flow. Moreover, at a Richardson number $\text{Ri} = \text{Gr}/\text{Re}^2 = 0.25$, buoyancy effects are non-negligible.

For a reference temperature $T_{\text{ref}} = 220°C$, thermo-physical properties of LBE can be calculated from correlations reported in Sobolev et al. (2011). By selecting the jet width $d = 1.5 \times 10^{-2}$m, which matches the order of magnitude of the PLAJEST experiment by Kimura et al. (2007), the chosen Gr-value issues $\Delta T = 72.7$°C, for which it results that $\Delta\rho/\rho \leqslant 0.9\%$, and hence the Boussinesq approximation holds, (see Kundu et al., 1990).

5.2. Numerical methodology

Numerical simulations are performed using Incompact3d (Laizet and Lamballais, 2009; Laizet and Li, 2011). It solves the incompressible Navier-Stokes equations together with a passive scalar transport equation on Cartesian grids. A third-order Runge-Kutta time integration scheme is used for the present study. As Incompact3d originally implements only passive scalar transport, the buoyancy term has been implemented for the present study. Also, inflow and outflow boundary conditions have been developed specifically, (see Fregni et al., 2019).

Periodic boundary conditions are set along the cross-flow y and the homogenous z directions. On the inflow plane ($x = 0$) velocity and

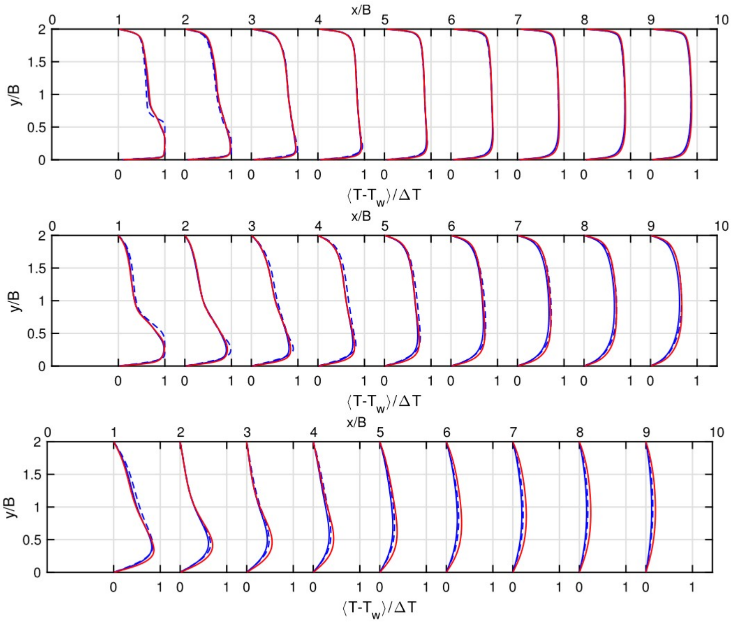

Fig. 16. Mean temperature profiles $(T - T_w)/\Delta T$ at $Pr = 1$ (top), 0.1 (middle) and 0.01 (bottom): L4000 (blue dash), T4000 (blue solid) and T5700 (red). (For interpretation of the references to colour in this figure legend, the reader is referred to the web version of this article.)

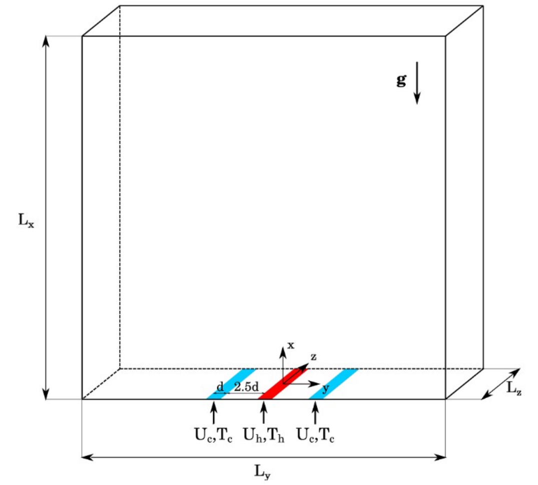

Fig. 17. Triple jet case: three-dimensional representation of the flow configuration.

temperature are set equal to zero at the solid wall, while in the three slots u, v, w and θ are assigned using snapshots recorded from a precursor channel simulation. The mean dimensionless fluid excess temperature of the hot jet centerline is $\theta_h = 0.5$, while for the lateral jets $\theta_c = -0.25$. Thus, the net inflow of thermal energy is zero. The fluid excess temperature is defined so that buoyancy forces vanish for $\theta = 0$ ($T = T_{\text{ref}}$). In the $x = L_x$ plane, outflow conditions are enforced on both the velocity and thermal fields.

Snapshots required to set inlet condition in the triple jet simulation are recorded from a DNS of the fully developed turbulent channel flow, where the temperature is computed as a passive scalar, with imposed heat flux at the walls. Snapshots of the velocity and temperature fields are saved on a cross flow plane every time step and then interpolated onto the $n_y \times n_z = 69 \times 512$ mesh of the jet slots. To uncorrelate the three inflows, a phase-shift is introduced between the three jets, the time shift considered is more than twice the integral time scale of the streamwise velocity component. In this way, the inflow turbulence is realistically generated rather than reproduced by synthetic methods.

The outflow condition enforced for the present study is developed by Stevens (1990) and reviewed by Hattori et al. (2013). This condition is based upon the one dimensional advection-diffusion equation:

$$\frac{\partial \phi}{\partial t} + \left(U_p + U_s\right)\frac{\partial \phi}{\partial x} = \chi \frac{\partial^2 \phi}{\partial x^2} \tag{2}$$

where χ represents the kinematic or thermal diffusivity, U_s is a vertical advection velocity and U_p is a phase velocity, which is computed using the generic quantity ϕ:

$$U_p \equiv \frac{\phi^{(n)}_{n_x-1} - \phi^{(n-1)}_{n_x-1}}{\phi^{(n-1)}_{n_x-2} - \phi^{(n-1)}_{n_x-1}}, \quad U_s \equiv \frac{u^{(n)}_{n_x} + u^{(n)}_{n_x-1}}{2} \tag{3a,b}$$

In definitions (3a,b), ϕ indicates either a velocity component or the fluid excess temperature θ, superscripts indicate time levels and n_x denotes the grid node at the outflow plane. In addition, it is prescribed to clip the sum $U_p + U_s$ so to ensure that

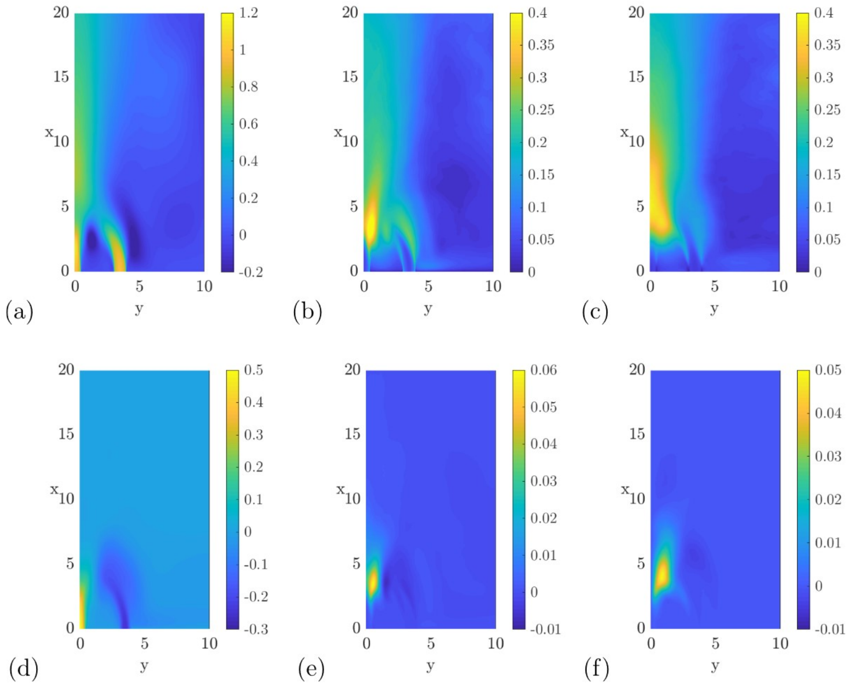

Fig. 18. Triple jet case: contours of (a) average streamwise velocity component $\langle u \rangle$; (b) root-mean-square of streamwise velocity fluctuations u_{rms}; (c) root-mean-square of cross-flow velocity fluctuations v_{rms}; (d) mean fluid exccess temperature $\langle \theta \rangle$; (e) streamwise component of turbulent heat flux $\langle u'\theta' \rangle$; (f) cross-flow component of turbulent heat flux $\langle v'\theta' \rangle$.

$$0 \leqslant U_p + U_s \leqslant U_j + U_{ff} \tag{4}$$

where U_{ff} is the maximum velocity related to the buoyancy effect, equal to $Ri^{0.5}$ in dimensionless form.

The simulation is performed on a domain of dimensions $L_x \times L_y \times L_z = 30d \times 30d \times 6d$, discretized by $2049 \times 2048 \times 512$ equally-spaced grid points. The computational time step is $\Delta t = 0.0005\,d/U_j$. The smallest turbulence scales computed *a posteriori* on the flow domain are: Kolmogorov length scale $\eta_{\min}/d = 3.86 \times 10^{-3}$ and Kolmogorov temporal scale $\tau_{\min}\,U_j/d = 7.43 \times 10^{-2}$. Grid spacing in the x and y directions equal $\Delta x = \Delta y = 3.8\eta_{\min}$, while $\Delta z = 3.0\eta_{\min}$. The timestep used corresponds to $\Delta t \approx 6.7 \times 10^{-3}\tau_{\min}$ and it is in fact selected on the basis of numerical considerations.

5.3. Selected results

In Fig. 18, a selection of statistics is reported, values are given in their non-dimensional form, (see Fregni et al., 2019) for the mathematical formulation and reference quantities. For convenience, data are presented in a region smaller than the computational domain, $(x, y) \in [0, 20] \times [0, 10]$. The statistics are calculated considering that the flow is homogeneous in time and along the spanwise direction (z). In addition, symmetry or antisymmetry has been exploited depending on the variable considered (u, w and θ are symmetric, while v is antisymmetric). Fig. 18(a) displays the mean streamwise velocity component. Induced by buoyancy the central jet accelerates, while the lateral ones decelerate and deviate towards the centreline. Regions of negative streamwise velocity are observed at the sides of the cold jets. This is due both to continuity and buoyancy effects where $\langle\theta\rangle < 0$. About $x \approx 6$, the three jets coalesce in a single stream.

Figs. 18(b) and (c) show fluctuations of the velocity components. Fluctuation intensities of the flow exiting the three slots rapidly evolve to much larger values and exhibit peaks where the three jets coalesce. Velocity fluctuations in y-direction undergo a larger increase with respect to fluctuations along x.

The average fluid excess temperature field is displayed in Fig. 18(d). Close to the inlets high temperature gradients are observed, while for $x > 6$ temperature variations are bounded by $|\Delta\theta| < 0.1$. Thus, far enough from the inlet, buoyancy effects become negligible and the flow behaves as purely mechanical. Figs. 18(e) and (f) display turbulent heat fluxes in vertical and cross-flow directions. Turbulent heat transfer is shown to substantially increase in the pool, and peaks are found in the mixing region, $x < 6$.

6. Shear layer

6.1. Flow configuration

The selected flow configuration is a time-evolving shear layer and is simulated in a 3D rectangular domain which is periodic in the directions parallel to the shear layer (x and z). In the normal direction (y), the domain is much larger than the shear layer and slip-wall boundary conditions are applied on the top and bottom surfaces. The domain size is L × H × W and is given in Fig. 19. Since the time-evolving shear layer is homogeneous in x and z, only the velocity difference $\Delta U = U_1 - U_2$ is important and it is usually simulated in a reference frame such that $U_1 = -U_2$. The initial mean velocity profile is $u = (\Delta U/2)\tanh(2y/\delta_{\omega,0})$; where ΔU is the velocity difference across the shear layer and $\delta_{\omega,0}$ is the initial vorticity thickness defined by $\delta_{\omega,0} = \Delta U / (\delta u/\delta y)_{max}$. A small perturbation is added to the velocity profile. The initial temperature profile is $T = (T_1 + T_2)/2 + (\Delta T/2)\tanh(2y/\delta_{\omega,0})$ where $\Delta T = T_1 - T_2$ is the temperature difference across the mixing layer, and no temperature perturbation is added.

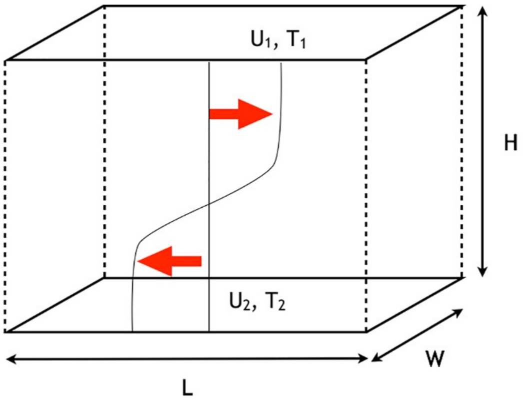

Fig. 19. Computational setup of the time-evolving shear layer.

6.2. Numerical methodology

The shear layer at Pr = 1–0.1–0.01 is simulated for three Reynolds numbers: $Re = \delta_{\omega,0}\Delta U/\nu = 700–2000–4000$. Because the objective was to achieve a Reynolds number as high as possible, a relatively small domain, similar to that used by Watanabe et al. (2016) and Watanabe and Nagata (2019), was selected, even though it does not allow to obtain fully converged statistics. However, for the lower Re = 700 case, a much larger domain was used and the results were ensemble-averaged over 9 simulations in order to obtain better statistics. The parameters of the simulations are provided in Table 3. In all cases, the initial perturbation was a diffused random noise (Kempf et al., 2005) with amplitude $U_{rms} = 0.01\,\Delta U$ and length scale $L_p = 0.25\,\delta_{\omega,0}$.

These shear layer simulations are performed using finite difference solver developed at UCLouvain. This code is also used for the impinging jet case and is described earlier in this article.

6.3. Selected results

The evolution of the shear layer is characterized by three phases: the laminar phase, the transition phase where instabilities grow and saturate, and eventually the turbulent phase. A turbulent self-similar shear layer should grow linearly (Pope, 2000). The obtained growth is indeed approximately linear in the turbulent regime. The evolution of the 75% velocity and temperature thicknesses of the mixing layer is presented in Fig. 20 for Re = 700 and 4000. As the Reynolds number increases, the difference between the thermal thickness at Pr = 0.01 and those at Pr = 1 and 0.01 decreases significantly. At Re = 4000, they eventually become equal at the very end of the simulation, however, this occurs in the phase where the growth is also significantly affected by the limited domain size. Yet, this shows that, if the Reynolds number is high enough, the thermal layer thickness becomes independent of the Prandtl number since the turbulent mixing becomes dominant over the molecular one.

Statistics were gathered in time windows where sufficient self-similarity was achieved. The mean profiles of velocity and temperatures are found to be very similar in all cases (see Fig. 21). The self-similar mean temperature profiles seem to exhibit a weak double inflexion shape whose origin is not completely clear and would require further investigation. The profiles of fluctuations for the velocity and for the temperatures at Pr = 1 and 0.1 (see Fig. 21) are quite close at the three Re and therefore likely correspond to the converged self-similar profiles. At low Prandtl, however, the amount of fluctuations is much lower than at Pr = 1 or 0.1 and it increases as the Reynolds number increases.

Table 3
Shear layer simulation parameters.

Re	$L/\delta_{\omega,0} \times H/\delta_{\omega,0} \times W/\delta_{\omega,0}$	$N_x \times N_y \times N_z$	$\Delta x/\eta$	$\Delta y_{min}/\eta$	$\Delta y_n/\eta$
700	136 × 150 × 90.66	1024 × 1024 × 512	2.7	0.7	3.6
2000	42.5 × 75 × 19.12	1024 × 1024 × 512	1.9	1.1	1.6
4000	42.5 × 75 × 19.12	2048 × 2048 × 1024	1.7	0.9	1.4

The ratio between the turbulent flux to the total heat flux increases with both the Reynolds and Prandtl numbers (see Fig. 21). At Pr $= 1$, it is very close to 1 for all the Re numbers. At Pr $= 0.1$, it is always larger than 0.9 but still slightly increases with Re. At Pr $= 0.01$, the maximum ratio grows from 0.5 to 0.85 in the range of investigated Reynolds numbers. The turbulent Prandtl number is an important quantity for RANS modelling. The obtained profiles (see Fig. 21) for Pr $= 1$ and 0.1 are almost identical and independent on the Re number. It is almost flat and equals to 0.7 in the center and steadily increases towards 0.9 at the edge of the shear layer. For Pr $= 0.01$, the profile is not flat at Re $= 700$ because the thermal layer is larger than the velocity layer. However, it becomes much flatter at Re $= 4000$ when the difference of layer thickness decreases. The center value is about $Pr_t = 1.0$ for the three Prandtl numbers.

The present simulations allowed to characterize the heat transfer in turbulent shear layers. A universal high Reynolds self-similar behaviour was clearly achieved for the velocity and for Pr $= 1$. However, at low Prandtl, such Re-independent self-similarity was not obtained because the shear layer probably never achieves a true self-similar regime until it has grown so much that the turbulence totally dominates the heat transfer. However, with a turbulent flux which account for up to 85% of the total flux, the present Re $= 4000$ simulation provides a good estimation of this behaviour and, in that case, the turbulent Prandtl number takes values close to 1 in the bulk of the shear layer.

7. Bare rod bundle

7.1. Flow configuration

The case under consideration is schematised in Fig. 22. An infinite triangular lattice of rods of diameter D is considered, whose centers are spaced by a pitch P, with $P/D = 1.4$. Each rod is considered as uniformly heated with a constant heat flux q". In the present work, a rectangular cell consisting of 4 subchannels (highlighted in Fig. 22) is considered. The particular choice of the P/D parameter comes from the work of Marinari et al. (2017), who performed a pre-test analysis of an experimental campaign on flow blockage in an LBE-cooled triangular array of rods. Based on the wide test matrix foreseen for their experiment, a single value of the friction Reynolds number has been chosen for the DNS, i.e. $\mathrm{Re}_\tau = 550$. Forced and mixed convection conditions have been considered. In the mixed convection case, the Richardson number imposed is $R_i = 0.22$. The Prandtl number is fixed to Pr $= 0.031$, corresponding to LBE at a reference temperature $T_{ref} = 220\,^\circ\mathrm{C}$, (see Sobolev et al., 2011).

7.2. Numerical methodology

The numerical technique adopted is based on a Finite Volume implementation of a second order Projection Method, following (Gresho, 1990). Time-discretizations of the conservation equations are performed according to a three-level scheme, which is semi-implicit (explicit in the streamwise direction x) for the diffusive terms and explicit Adams-Bashforth for the advective terms. Such a practice is second order accurate in time.

Spatial derivatives are approximated with second order central differences on staggered Cartesian grids, which can be non-uniform on the transverse $y - z$ plane. A fast direct resolution of the discrete momentum and energy equations at each time-step is made possible by means of Approximate Factorization, while the Poisson problem associated with the pressure-velocity coupling (Gresho, 1990) is solved through a fast Poisson solver, based on Matrix Decomposition.

The modelling of arbitrarily irregular cylindrical boundaries on Cartesian grids is achieved, thanks to the original scheme developed by Barozzi et al. (2004) and extended to convective problems by Angeli et al. (2015) and Angeli and Stalio (2019). The technique involves a local modification of the computational stencil where boundary segments intersect the stencil arms. The method has been implemented in a parallel, highly efficient in-house code. A validation of the code against literature DNS data and an assessment of its computational performances can be found in Angeli and Stalio (2019).

The computational domain size considered is $8\pi D_h \times 1.2 D_h \times 2.1 D_h$, where

$$D_h = \left[\frac{2\sqrt{3}}{\pi}\left(\frac{P}{D}\right)^2 - 1\right] D \tag{5}$$

is the hydraulic diameter of a subchannel. For the present case, $D_h \simeq 1.16D$. The domain in the crossflow direction is such that it encompasses four subchannels. The number of control volumes along the three directions is $2048 \times 448 \times 256$. A constant spacing has been kept along all directions, corresponding, in wall units, to

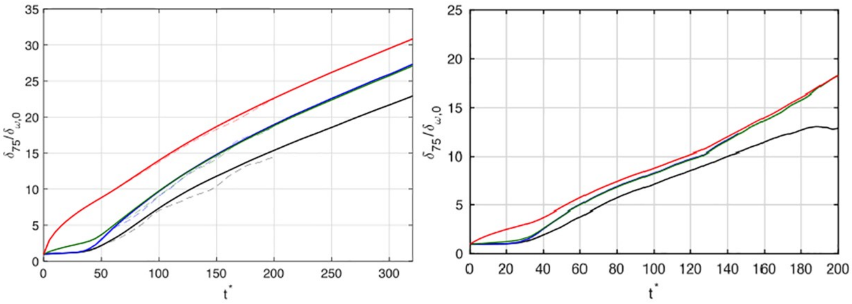

Fig. 20. Comparison of the δ_{75} velocity thickness (black) and of the $\delta_{T,75}$ temperature thicknesses at Pr $= 1$ (blue), 0.1 (green) and 0.01 (red): Re $= 700$ (Left) and Re $= 4000$ (Right) simulations.

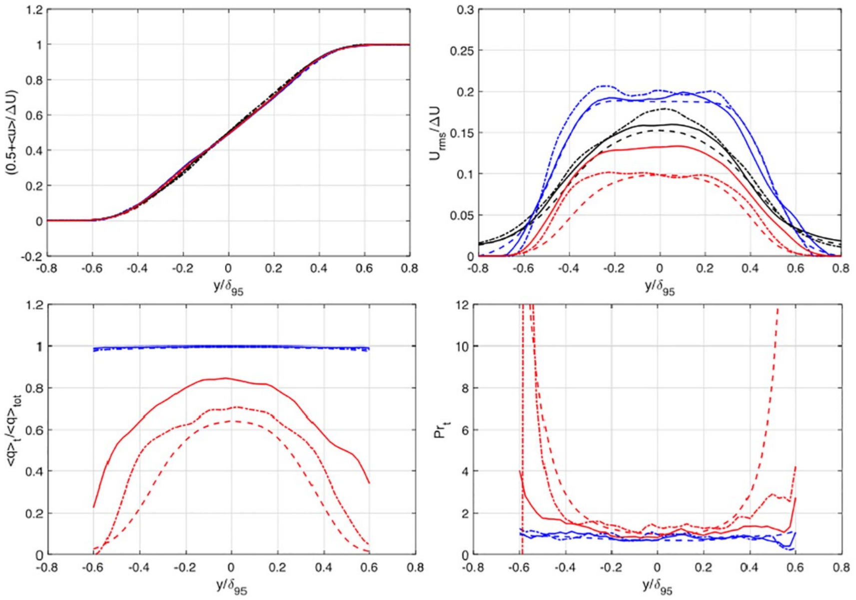

Fig. 21. Mean self-similar velocity (0.5 + u/ΔU) or temperature T-T2/ΔT profiles (top left), mean velocity $U_{rms}/\Delta U$ or temperature $T_{rms}/\Delta T$ fluctuations (top right), Ratio of the turbulent flux to the total flux (bottom left) and turbulent Prandtl number (bottom right): Re = 700 (dash), 2000 (dash-dot) and 4000 (solid), Velocity (black), temperature at Pr = 1 (blue) and Pr = 0.01 (red). Each profile is normalized using its own $\delta_{T,95}$. (For interpretation of the references to colour in this figure legend, the reader is referred to the web version of this article.)

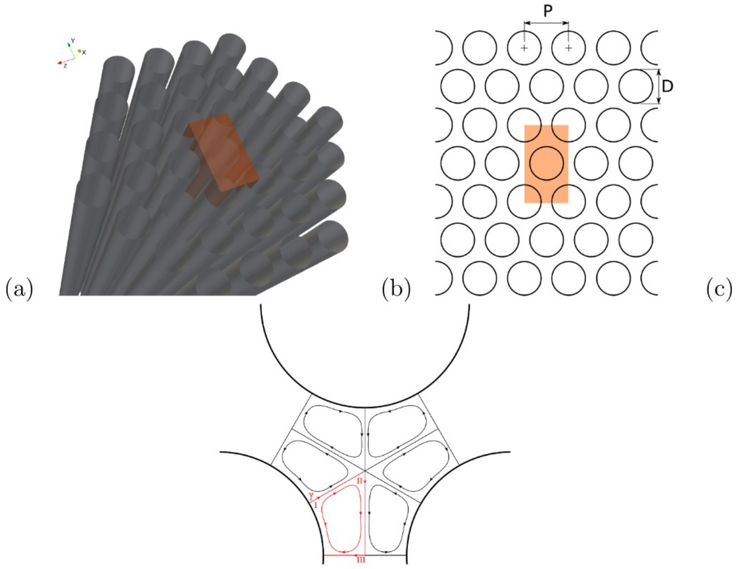

Fig. 22. Bare rod bundle DNS: (a) 3D representation of a triangular bundle; (b) crossflow layout with periodic rectangular module highlighted, comprising four subchannels; (c) unit flow cell.

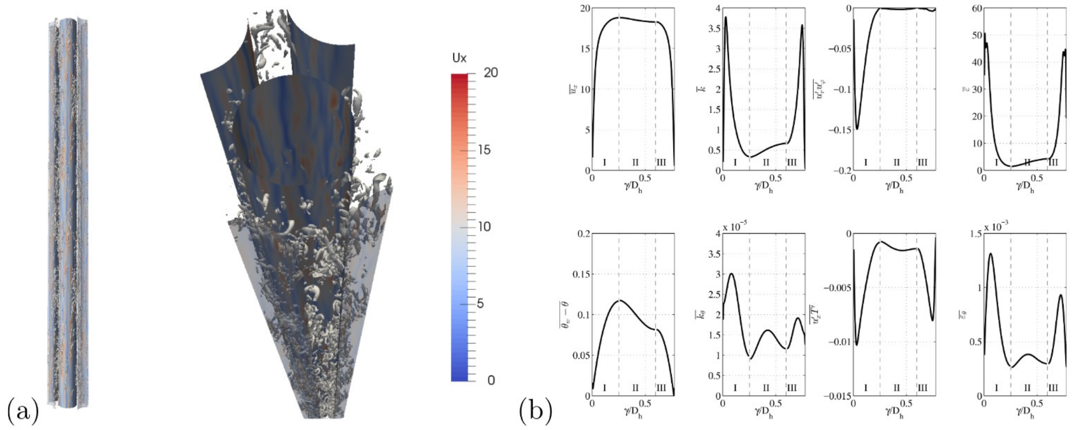

Fig. 23. Bare rod bundle DNS at $\mathrm{Re}_\tau = 550$, Ri $= 0.22$: (a) contours of the instantaneous streamwise velocity component at $y^+ \approx 10$, and isosurfaces of Q around the vertical pins; (b) profiles of $\overline{u_x}$, $\overline{\theta_w - \theta}$, $\overline{k}$, $\overline{k_\theta}$, $\overline{u'_r u'_\varphi}$, $\overline{u'_x \theta'}$, $\overline{\varepsilon}$ and $\overline{\varepsilon_\theta}$ across the unit flow cell border.

$y^+_{wall} \approx 0.3$, $\Delta y^+ \approx 2.5$, $\Delta z^+ \approx 6$.

Concerning boundary conditions, the physical situation of a bundle of heated rods under the hypothesis of fully developed flow and heat transfer can be well represented through periodic conditions enforced on the velocity field and the modified pressure field p_m. Furthermore, the temperature field needs to be normalized so that periodic boundary conditions can be also set on a modified temperature-like variable θ, (see Piller et al., 2014).

7.3. Selected results

A selection of results is reported here on the mixed convection case with $\mathrm{Re}_\tau = 550$ and Ri $= 0.22$. Contours of the instantaneous streamwise velocity field at $y^+ \approx 10$ magnitude are shown in Fig. 23(a), together with structures visualized via iso-surfaces of the Q-criterion (Hunt et al., 1988). The Q-criterion defines a vortex as a connected fluid region with a positive second invariant of $\nabla \mathbf{u}$ (Hunt et al., 1988). In other words, Q represents the local balance between shear strain rate and vorticity magnitude, defining vortices as areas where the vorticity magnitude is greater than the magnitude of the rate-of-strain. In Fig. 23(a), streaks of fast moving fluid particles are observed in the regions close to the heated cylinders, alternating with low-speed streaks.

Fig. 22(c) schematizes the overall structure of the flow in a subchannel. As acquainted above, under the hypothesis of fully-developed flow, all the variables whose time-averaged behaviour in the streamwise direction is known are normalized in order to be able to impose periodic boundary conditions in the streamwise direction and, hence, treat such direction as homogeneous (Piller et al., 2014). Therefore, statistics do not depend anymore on the streamwise coordinate and the average fields become 2D. Furthermore, exploiting the inherent symmetry of the domain, statistics can be reduced to the unit flow cell corresponding to one sixth of the base subchannel. 1D profiles are also carried out along the contour of the unit cell, corresponding to the sum of the largest (parts I and II) and the smallest (part III) path connecting two rods.

Contours of the average streamwise velocity component $\overline{u_x}$, wall-bulk temperature difference $\overline{\theta_w - \theta}$ and Pr_t on the unit flow cell are reported in Fig. 24, alongside with streamlines of the cross-flow components. The buoyancy-induced flow in these geometries is seen to be characterized by non-zero time-averaged secondary flows. The circulation is driven towards the rods in the narrowest gap, while it is directed towards the center of the subchannel in the largest gap.

Profiles of relevant quantities along the curvilinear abscissa γ are reported in Fig. 23(b). Overall, it is to be noted that the low Pr-value determines very small fluctuations of θ and an analogously small dissipation rate of temperature fluctuations. Near-wall peaks of turbulent kinetic energy, Reynolds stresses of cross-flow components and turbulent dissipation rate are instead found.

8. Infinite wire-wrap

8.1. Flow configuration

The selected flow configuration is an infinite wire-wrapped (IWW) fuel assembly. It is based on the dimensions of the MYRHHA design, which are given in Table 4. It is worth mentioning that the MYRHHA fuel assembly consists of 127 wire-wrapped fuel pins, and to generate a benchmarking CFD database of a fuel assembly would require enormous computational resources and is not foreseeable in the near future. Hence, an extensive RANS study was performed by Shams et al. (2015) in order to design an IWW fuel pin, which can represent the realistic MYRHHA fuel design without wall effects and yet it is feasible for the available computational resources. For more details, (see Shams et al., 2015).

This geometric design of the IWW is shown in Fig. 25. This flow configuration represents a periodic domain, allowing to numerically impose periodic boundary conditions to their respective opposite sides, as highlighted in Fig. 25. The length of the computational domain is kept to one wire wrap pitch, which also allows imposing periodic boundary conditions in the principal flow direction. Thus, the selected single rod wire-wrapped domains result in an infinite rod bundle domain. Liquid LBE is considered as a working fluid with an average inlet temperature (T_{inlet}) of 340 °C. This results in the Pr $= 0.02$. The imposed Reynolds number (based on the hydraulic diameter) for the selected computational domain is Re $= 7015$, which corresponds to a computed friction Reynolds number (Re_τ) of 459. Moreover, a constant heat flux, $Q = 0.152\ \mathrm{MW/m^2}$ has been imposed on the main rod. For more details (see Shams et al., 2018).

8.2. Numerical methodology

The commercially available STAR-CCM + code, version 10.02 (STAR-CCM +, 2013), is used to perform this high-fidelity simulation. Following the work of Shams et al. (2013), no turbulence model is used to perform this high fidelity simulation. A second order central scheme

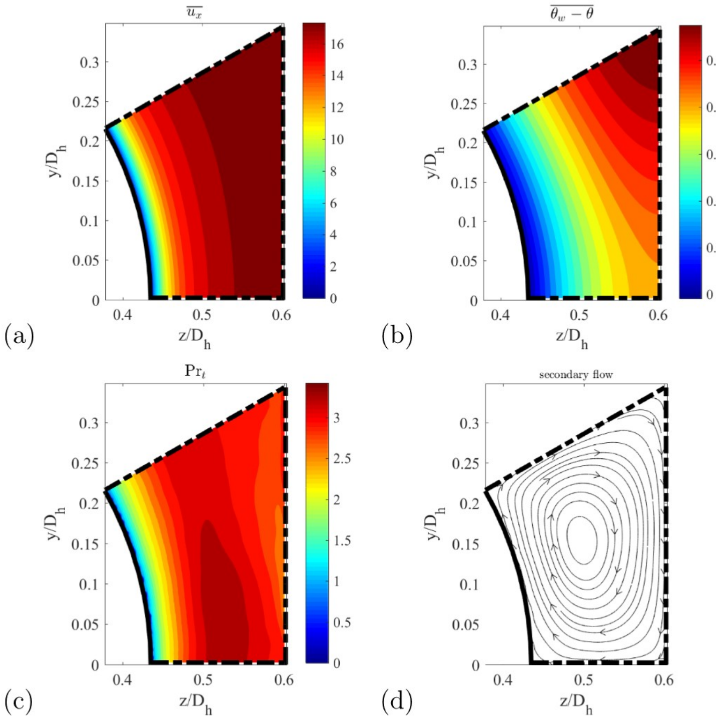

Fig. 24. Bare rod bundle DNS at $\mathrm{Re}_\tau = 550$, $\mathrm{Ri} = 0.22$: Contours of time-averaged (a) $\overline{u_x}$, (b) $\overline{\theta_w - \theta}$ and (c) Pr_t on the unit flow cell and (d) streamlines of the mean secondary flow components.

Table 4
Dimensions of the infinite wire-wrapped rod bundle based on the MYRHHA design.

Parameters	Values	Units
Diamter of the rod	6.55	mm
Diamter of the wire	1.75	mm
Wire (wrapping) pitch	262	mm
Gap (between wire and rod)	0.1	mm

with 5% boundedness has been used for the spatial discretization. Generating a high quality mesh for high fidelity simulation reference simulations traditionally requires a hexahedral type meshing to keep the numerical dissipation to the minimal. However, to generate a hexahedral mesh for such a complex flow configuration poses severe restrictions. Therefore, a polyhedral meshing technique is chosen to generate the final mesh. In the near wall region, a structured prism layer mesh is generated to correctly capture the near wall high flow gradients. The overall aspect ratio of the mesh is kept around 1.05 to

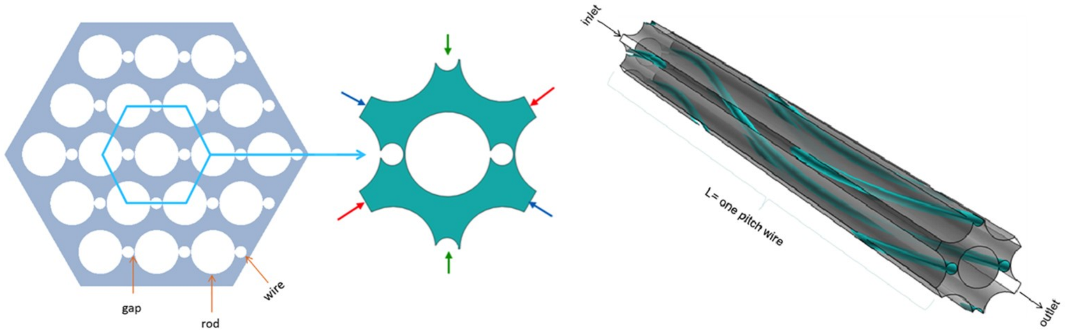

Fig. 25. Domain selection based on a larger (19 pin wire-wrapped) domain. The selected infinite wire-wrap domain: green, red and blue arrows indicate respective periodic sides (Shams et al., 2018).

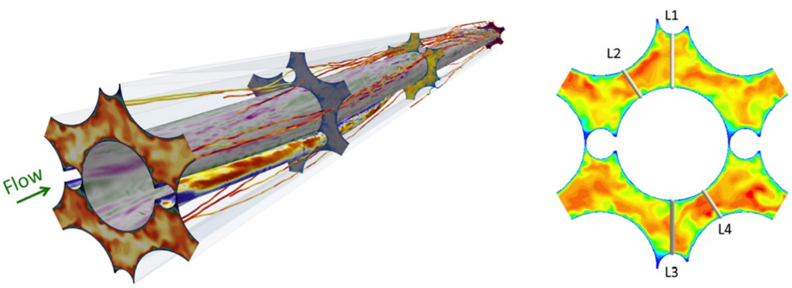

Fig. 26. (left) isometric view of the predicted flow feature appearing in the computational domain (right) iso-contours of instantaneous velocity field (along with the selected four lines) at the mid cross-section of the domain (Shams et al., 2018).

ensure the good quality for the numerical results. Additionally, special care has been taken to generate a smooth transition from the smooth prism layer (in the near wall region) to the bulk region. Based on a priori RANS results, an estimation of the Kolmogorov length scales appearing in this flow configuration was performed. Accordingly, following the DNS guidelines (see Shams et al., 2018), the mesh was generated and resulted in a total of 42 million cells. The non-dimensionalized cell sizes of this generated mesh are ($\Delta x^+_{max} = 7$, $\Delta y^+ = 0.5$–7, $\Delta z^+_{max} = 7$). These cell sizes are much finer than the estimated Kolmogorov's legth scale (KLS) from the RANS computation. Nonetheless, when such a mesh is used in STAR-CCM + to perform a DNS, it should be called a quasi-DNS (q-DNS) merely because of the reason that at maximum second order schemes will be used to perform the simulations. These numerical schemes were also used and tested in the study of Shams et al. (2013) and Komen et al. (2014). They show that the results of such a q-DNS are in excellent agreement with a generally accepted high quality DNS databases. Furthermore, a second order, implicit three time level scheme is used for temporal discretization.

8.3. Selected results

Fig. 26 (left) displays an isometric view of the obtained solution. The complexity of the flow regime is highlighted by the streamlines in the axial flow direction, contours of instantaneous wall shear stresses over the wire and the main rod, and cross-sectional contours of the instantaneous velocity and temperature at various axial locations through the computational domain. Validating the low-order

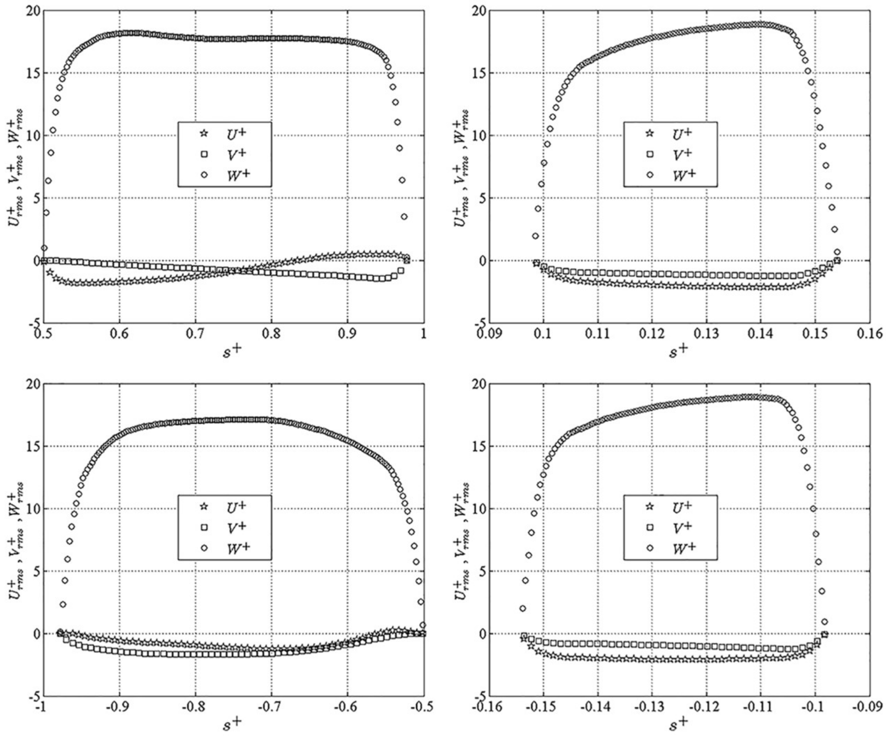

Fig. 27. Time-averaged velocity profiles for the line (top: left) L1, (top: right) L2, (bottom: left) L3 and (bottom: right) L4.

turbulence modelling approaches could be challenging for such a complex flow configuration. Therefore, a well-defined extensive database has been generated including the temperature and the thermal fields (mean and RMS) over the main rod; mean and RMS of velocity and temperature, Reynolds stresses and turbulent heat fluxes at the mid cross-section of the computations domain, for details (see Shams et al., 2018). For the sake brevity, only time-averaged velocity profiles for L1, L2, L3 and L4 (as highlighted in Fig. 26 (right)) are given in Fig. 27.

9. Summary and conclusions

In the framework of the EU SESAME and MYRTE projects, an extensive effort has been put forward to generate a wide range of reference data, both experimental and numerical, to help validating and/or further development of available turbulent heat flux models. This article reports the numerical database that has been generated within these projects for various liquid metal flow configurations in different flow regimes. These high fidelity numerical data include seven different flow configurations:

1. a wall-bounded mixed convection planar channel flow at Prandtl number (Pr) = 0.025 and the Reynolds number (Re) = 4665. The influence of the mixed convection has been studied by varying the Richardson number (R_i) = 0, 0.25, 0.5 and 1.
2. a forced convection confined backward facing step (BFS) with a conjugate heat transfer. This BFS has been studied at the Re = 7089 for the Pr = 0.005. The ratio of the conductivities of the fluid and the solid material was set to 3.
3. a forced convection impinging jet case for three different Prandtl fluids, i.e. Pr = 1, 0.1 and 0.01. This impinging jet has been studied for three different inlet conditions, i.e. a laminar inflow with Re = 4000 and fully developed planar turbulent jets for Re = 4000 and 5700.
4. a mixed-convection cold-hot-cold triple jet configuration corresponding to R_i = 0.25. The Re number of each jet is equal to 5000 and the Pr number of the working fluid was kept equal to 0.031.
5. an unconfined free shear layer for three different Reynolds numbers (Re = 700, 2000 and 4000) and each case has been studied for three different Prandtl fluids, i.e. Pr = 1, 0.1 and 0.01.
6. a wall-bounded mixed and forced convection flow in a bare rod bundle configuration for $\mathrm{Re}_\tau = 550$ at Pr = 0.031. For the mixed convection case, R_i = 0.22 has been imposed.
7. and a forced convection infinite wire-wrapped fuel assembly, whose geometric parameters are based on the MYRHHA design. This case was studied for the Re = 7015 and the corresponding Pr = 0.02.

These high-fidelity numerical databases will serve the further development of turbulent heat transfer models by providing unique, new and detailed data for the thermal-hydraulic behaviour of liquid metals in various flow configurations.

Declaration of Competing Interest

The authors declare that they have no known competing financial interests or personal relationships that could have appeared to influence the work reported in this paper.

Acknowledgements

The work described in this paper has been funded by the Euratom research and training program 2014–2018 under grant agreements No. 654935 (SESAME) and 6621865 (MYRTE).

References

Angeli, D., Stalio, E., 2019. A fast algorithm for direct numerical simulation of turbulent convection with immersed boundaries. Comput. Fluids 183, 148–159.

Angeli, D., Stalio, E., Corticelli, M., Barozzi, G., 2015. A fast algorithm for direct numerical simulation of natural convection flows in arbitrarily-shaped periodic domains. J. Phys: Conf. Ser. 655 (1), 012054.

Barozzi, G.S., Bussi, C., Corticelli, M.A., 2004. A fast cartesian scheme for unsteady heat diffusion on irregular domains. Numer. Heat Transfer B 46, 56–77.

Dairay, T., Fortune, V., Lamballais, E., Brizzi, L., 2014. Les of a turbulent jet impinging on a heated wall using high-order numerical schemes. Int. J. Heat Fluid Flow 50, 177–187.

Fischer, P., James, F., Lottes, W., Kerkemeier, S.G., 2010. Nek5000 web page, http://nek5000.mcs.anl.gov.

Flageul, C., Benhamadouche, S., Lamballais, E., Laurence, D., 2017. Les of a turbulent jet impinging on a heated wall using high-order numerical schemes. Int. J. Heat Fluid Flow 111, 321–328.

Fregni, A., Angeli, D., Cimarelli, A., Stalio, E., 2019. Direct numerical simulation of a buoyant triple jet at low-Prandtl number. Int. J. Heat Mass Transfer In Press.

Gresho, P.M., 1990. On the theory of semi-implicit projection methods for incompressible flow and its implementation via a finite element method that also introduces a nearly consistent mass matrix. part 1: theory. Int. J. Numer. Meth. Fluids 11, 587–620.

Grotzbach, G., 2013. Challenges in low-Prandtl number heat transfer simulation and modelling. Nucl. Eng. Des. 264, 41–55.

Hattori, H., Nagano, Y., 2004. Direct numerical simulation of turbulent heat transfer in plane impinging jet. Int. J. Heat Fluid Flow 25 (5), 749–758.

Hattori, T., Norris, S., Kirkpatrick, M., Armfield, S., 2013. Comparison of non-reflective boundary conditions for a free-rising turbulent axisymmetric plume. Int. J. Numer. Meth. Fluids 72 (12), 1307–1320.

Hunt, J., Wray, A., Moin, P., 1988. Eddies, streams, and convergence zones in turbulent flows, in: Proc. 1988 Summer Program, Stanford N.A.S.A. Centre for Turb. Res., cTR-S88.

Jaramillo, J., Trias, F., Gorobets, A., Pŕez-Segarra, C., Oliva, A., 2012. DNS and RANS modelling of a turbulent plane impinging jet. Int. J. Heat Mass Tran. 55 (4), 789–801.

Jung, J.H., Yoo, G.J., 2004. Analysis of unsteady turbulent triple jet flow with temperature difference. J. Nuclear Sci. Technol. 41 (9), 931–942.

Kasagi, N., Ohtsubo, Y., 1993. Direct numerical simulation of low Prandtl number thermal field in a turbulent channel flow. In: Turbulent Shear Flows, vol. 8. Springer, pp. 97–119.

Kays, W., 1994. Turbulent Prandtl number – where are we. J. Heat Transfer-Trans. ASME 116 (2), 284–295.

Kempf, A., Klein, M., Janicka, J., 2005. Efficient generation of initial- and inflow-conditions for transient turbulent flows in arbitrary geometries. Flow, Turbul. Combust. 74, 67–84.

Kim, J., Moin, P., Moser, R., 1987. Turbulence statistics in fully developed channel flow at low reynolds number. J. Fluid Mech. 177, 133–166.

Kimura, N., Miyakoshi, H., Kamide, H., 2007. Experimental investigation on transfer characteristics of temperature fluctuation from liquid sodium to wall in parallel triple-jet. Int. J. Heat Mass Transfer 50 (9–10), 2024–2036.

Komen, E., Shams, A., Camilo, L., Koren, B., 2014. Quasi-DNS capabilities of openfoam for different mesh types. Comput. Fluids 96, 87–104.

Kundu, P.K., Cohen, I., 1990. Fluid Mechanics. Academic Press.

Laizet, S., Lamballais, E., 2009. High-order compact schemes for incompressible flows: a simple and efficient method with quasi-spectral accuracy. J. Comput. Phys. 228 (16), 5989–6015.

Laizet, S., Li, N., 2011. Incompact3d: a powerful tool to tackle turbulence problems with up to o (105) computational cores. Int. J. Numer. Meth. Fluids 67 (11), 1735–1757.

Marinari, R., Di Piazza, I., Forgione, N., Magugliani, F., 2017. Pre-test cfd simulations of the nacie-up bfps test section. Ann. Nucl. Energy 110, 1060–1072.

Moser, R., Kim, J., Mansour, N., 1999. Direct numerical simulation of turbulent channel flow up to $re_\tau = 590$. Phys. Fluids 11 (4), 943–945.

Oliver, T.A., Malaya, N., Ulerich, R., Moser, R., 2014. Estimating uncertainties in statistics computed from direct numerical simulation. Physics of Fluids 26 (3), 035101. https://doi.org/10.1063/1.4866813. AIP Publishing.

Piller, M., Polidoro, S., Stalio, E., 2014. Multiplicity of solutions for laminar, fully-developed natural convection in inclined, parallel-plate channels. Int. J. Heat Mass Transf. 79, 1014–1026.

Pope, S. 2000, Turbulent flows.

Roelofs, F., Batta, A., Bandini, K., Van Tichelen, G., Gerschenfeld, A., Cheng, X., 2014. European liquid metal themal-hydraulics R&D: Present & Future. In: ENC, Marseille, France.

Roelofs, F., Shams, A., Otic, I., Böttcher, M., Duponcheel, M., Bartosiewicz, Y., Lakehal, D., Baglietto, E., Lardeau, S., Cheng, X., 2015. Status and perspective of turbulence heat transfer modelling for the industrial application of liquid metal flows. Nucl. Eng. Des. 290, 99–106.

Shams, A. 2017. (U)RANS: turbulence modelling, SESAME Project: Lecture Series on Thermohydraulics and Chemistry of Liquid Metal Cooled Reactors, von Karman Institute for Fluid Dynamics, 10th-14th April 2017.

Shams, A., 2018. The importance of turbulent heat transfer modelling in low-Prandtl fluids. In: Advances in Thermal Hydraulics (ATH 2018), ANS Winter Meeting

Embedded Topical, November, Orlando, FL.
Shams, A., 2019. Turbulent heat transport. In: book: Thermal Hydraulics Aspects of Liquid Metal Cooled Nuclear Reactors Woodhead Publishing, pp. 273–292.
Shams, A., Roelofs, F., Komen, E., Baglietto, E., 2013. Quasi-direct numerical simulation of a pebble bed configuration. part i: Flow (velocity) field analysis. Nucl. Eng. Des. 263, 473–489.
Shams, A., Roelofs, F., Baglietto, E., Lardeau, S., Kenjeres, S., 2014. Assessment and calibration of an algebraic turbulent heat flux model for low-Prandtl fluids. Int. J. Heat Mass Transf. 79, 589–601.
Shams, A., Roelofs, F., Momen, E., 2015. High-fidelity numerical simulation of the flow through an infinite wire-wrapped fuel assembly. In: The 16th International Topical Meeting on Nuclear Reactor Thermalhydraulics NURETH-16, Chicago, USA.
Shams, A., Roelofs, F., Komen, E., Baglietto, E., 2018. High fidelity numerical simulations of an infinite wire-wrapped fuel assembly. Nucl. Eng. Des. 335, 441–459.
Shams, A., De Santis, A., Koloszar, L., Villa-Ortiz, A., Narayanan, C., 2019. Status and perspectives of turbulent heat transfer modelling in low-prandtl number fluids. Nucl. Eng. Des. 353, 110220.
Sobolev, V. 2011. Database of thermophysical properties of liquid metal coolants for GEN-IV, Tech. Rep. BLG-1069, SCK-CEN, Belgium.
STAR-CCM+, User manual, cd adapco, london (2013).
Stevens, D.P., 1990. On open boundary conditions for three dimensional primitive equation ocean circulation models. Geophys. Astrophys. Fluid Dyn. 51 (1–4), 103–133.
Tiselj, I., 2014. Tracking of large-scale structures in turbulent channel with direct numerical simulation of low Prandtl number passive scalar. Phys. Fluids 26 (12), 125111.
Vasilyev, O., 2000. High order finite difference schemes on non-uniform meshes with good conservation properties. J. Comp. Phys. 157 (2), 746–761.
Watanabe, T., Nagata, K., 2019. Multi-particle dispersion during entrainment in turbulent free-shear flows. J. Comput. Phys. 350, 518–529.
Watanabe, T., da Silva, C., Nagata, K., 2016. Multi-particle dispersion during entrainment in turbulent free-shear flows. J. Fluid Mech. 805, R1.
Yu, Y., Merzari, E., Thomas, J.W., Obabko, A., Aithal, S., 2017. Steady and unsteady calculations on thermal striping phenomena in triple-parallel jet. Nucl. Eng. Des. 312, 429–437.